Feasibility of image quality improvement for high-speed CBCT imaging using deep convolutional neural network for image-guided radiotherapy in prostate cancer

Feasibility of image quality improvement for high-speed CBCT imaging using deep convolutional neural network for image-guided radiotherapy in prostate cancer

Tomoyuki Kurosawa,[a,b,*] Teiji Nishio,[a] Shunsuke Moriya,[b,c] Masato Tsuneda,[d] Kumiko Karasawa[d]

[a]Department of Medical Physics, Graduate School of Medicine, Tokyo Women's Medical University, Tokyo 1628666, Japan

[b]Particle Therapy Division, Research Center for Innovative Oncology, National Cancer Center, Chiba 2778577, Japan

[c]Doctoral Program in Biomedical Sciences, Graduate School of Comprehensive Human Sciences, University of Tsukuba, Ibaraki 3058577, Japan

[d]Department of Radiation Oncology, Tokyo Women's Medical University, Tokyo 1628666, Japan

***Corresponding author:** Tomoyuki Kurosawa

Department of Medical Physics, Graduate School of Medicine, Tokyo Women's Medical University, Tokyo 1628666, Japan

Tel. +81(3)3353-8111

E-mail: kuro.3.panch@gmail.com

Abstract

Purpose: High-speed cone-beam computed tomography (CBCT) scan for image-guided radiotherapy (IGRT) can reduce both the scan time and the exposure dose. However, it causes noise and artifacts in the reconstructed images due to the lower number of acquired projection data. The purpose of this study is to improve the image quality of high-speed CBCT using a deep convolutional neural network (DCNN).

Methods: CBCT images of 36 prostate cancer patients were selected. The CBCT images acquired at normal scan speed were defined as $CBCT_{100\%}$. Simulated high-speed CBCT images acquired at twofold and fourfold scan speed were created, which were defined as $CBCT_{50\%}$ and $CBCT_{25\%}$, respectively. The image quality of the $CBCT_{50\%}$ was treated as the requirement for IGRT in this study because previous studies reported that its image is sufficient with respect to IGRT. The DCNN model was trained to learn direct mapping from $CBCT_{25\%}$ to the corresponding $CBCT_{100\%}$. The performance of the DCNN model was evaluated using the sixfold cross-validation method. CBCT images generated by DCNN ($CBCT_{25\%+DCNN}$) were evaluated for voxel value accuracy and image quality.

Results: The DCNN model can process $CBCT_{25\%}$ of a new patient within 0.06 s/slice. The $CBCT_{25\%+DCNN}$ was comparable to the $CBCT_{50\%}$ in terms of both voxel value accuracy and image quality.

Conclusions: We developed a DCNN model to remove noise and artifacts from high-speed CBCT. We emphasize that it is possible to reduce exposure to one quarter and to increase the CBCT scan speed by a factor of four.

Key words: Radiotherapy, Cone-beam computed tomography, Image-guided radiotherapy, Convolutional neural network

1. Introduction

Image-guided radiotherapy (IGRT) in prostate cancer has become a standard treatment in therapies such as intensity modulation radiotherapy and volumetric modulation radiotherapy (VMAT), which deliver high-dose radiation. In particular, previous studies have shown that the use of daily IGRT in prostate cancer improves clinical target volume (CTV) coverage and reduces rectal dose, gastrointestinal toxicity, and urinary toxicity [1-5]. Currently, two IGRT modalities are mainly used for prostate cancer: a combination of a fiducial marker implanted in the prostate and orthogonal portal imaging and cone-beam computed tomography (CBCT). CBCT does not require an invasive procedure and can obtain three-dimensional information of target and normal organs. Daily IGRT using CBCT in prostate cancer has limitations in terms of exposure dose [6-8]. For example, if a dose of 2 cGy is delivered per scan during each of 40 fractions, it amounts to an accumulated dose of 0.8 Gy over the course of treatment [8]. Furthermore, a CBCT scan requires approximately 60 to 120 s because projection data are continuously acquired while a linear accelerator (linac) gantry is rotated at a constant speed of approximately 3–6 deg/s. Extension of the total treatment time not only increases the probability of patient position error but also decreases patient throughput [9, 10]. High-speed CBCT scan has been proposed to solve these problems [11-14]. Acquisition times can be reduced by increasing the gantry rotation speed. In addition, dose reduction can be realized because the frequency of the projection data acquisition is constant [11, 13]. However, it has been reported that a high-speed CBCT scan causes significant noise and several artifacts in the CBCT images owing to the lower number of acquired projection data. This significantly affects the IGRT accuracy [11, 13]. Westberg et al. [11] evaluated the accuracy of IGRT in high-speed CBCT images. The projection data were processed (sub-sampling and reconstructing) to simulate high-speed CBCT images by sub-sampling and reconstructing projection data to simulate high-speed CBCT images. They reported that IGRT accuracy did not decrease in the case where the number of projection data is more than 50% of the original data. If the number of projection data is reduced to 25% of the original data, artifacts become significant and affect IGRT accuracy by more than 1 mm at maximum.

We applied a deep convolutional neural network (DCNN) to remove noise and artifacts from high-speed CBCT images. Currently, several deep learning algorithms have been proposed to improve image quality [15-22]. In particular, DCNNs are powerful techniques

for feature extraction and they have been applied to image denoising and artifacts reduction. For example, Kida et al. proposed a technique to improve the image quality of CBCT images by applying a DCNN to learn mappings from CBCT images to their corresponding planning CT images [21]. Zhang et al. used a DCNN-based approach to reduce metal artifacts on CT images [17]. In this study, we developed a DCNN-based method to reduce the noise and artifacts from high-speed CBCT images and evaluated its effectiveness.

2. Materials and methods

2.1. Data acquisition and processing

Thirty-six prostate cancer patients treated with VMAT were selected. CBCT datasets were acquired using the X-ray Volumetric Imager (XVI) of the Elekta Synergy (Elekta, Stockholm, Sweden) system (version 4.2.2) at the first day of the treatment. Table 1 shows the acquisition parameters. All CBCT datasets were reconstructed over a 410 mm × 410 mm × 120 mm volume at a resolution of 1.0 mm.

In this study, we created post-processed reconstruction data from XVI to mimic high-speed CBCT images. Figure 1 shows the procedure for reconstructing each CBCT image. First, the original CBCT images were projected using the Radon transform, and 480 imaginary projection data at angles from 0° to 360° were created. Three types of CBCT images were then reconstructed from the projection data. We defined the CBCT images reconstructed from 480 projection data (all projection data) as $CBCT_{100\%}$. By sub-sampling the projection data in ratios of 1:2 and 1:4, $CBCT_{50\%}$ and $CBCT_{25\%}$ were reconstructed, respectively. Here, the projection data were evenly subsampled over the initial set of projections. $CBCT_{50\%}$ and $CBCT_{25\%}$ mimicked high-speed CBCT images acquired at twofold and fourfold gantry rotation speeds, respectively. All the CBCT images were reconstructed using the filtered back projection with parallel-beam geometry based on the scikit-image image processing library [23]. Because the accuracy of $CBCT_{50\%}$ is sufficient with respect to IGRT [11], its image quality was treated as the requirement for IGRT in this study.

2.2. DCNN architecture

Previous studies have shown that the network receptor field must be sufficiently large and deep to capture artifacts that spread throughout images [18, 21, 22]. We modified the network as shown in Figure 2. The hyper parameters were optimized by minimizing the absolute error between the predicted images and the corresponding ground truth images. The front end of the network has a pooling layer that is used after each stage, while the back end uses an up-sampling layer. It has a shortcut to link the results from the front end of the network to the back end. The network uses a total of 18 convolution layers and rectified linear units, and we applied zero padding so that the image size does not decrease after passing through the convolution layer. This model was implemented using TensorFlow and Keras as the backend.

2.3. Sixfold cross-validation of U-net CNN model

The performance of the constructed U-net CNN model was evaluated using the sixfold cross-validation method because the sample size was small. The CBCT datasets of six patients were used as a test set each time, and the CBCT datasets of the remaining 30 patients were used as training data for the model per slice. CBCT images of all slices (120 slices/patient) were used for DCNN training. Data augmentation was performed before the training process to increase the amount of training data, and randomly translated images were added to the training data. After applying augmentation, the number of training subjects increased from 30 to 90, yielding a total of 10,080 paired $CBCT_{25\%}$–$CBCT_{100\%}$ slices. A binary body mask was applied to all CBCT images to extract their body regions. This procedure was achieved by applying the Otsu auto-thresholding method on each CBCT image, and the voxel values outside the mask region were entirely replaced by zero. A pair of images of $CBCT_{25\%}$ and $CBCT_{100\%}$ was normalized to a voxel value in the range of zero to one.

Training was performed by minimizing the loss function defined as the mean absolute error of pixel values between $CBCT_{100\%}$ and CBCT images generated by DCNN ($CBCT_{25\%+DCNN}$). Using the Adam optimization algorithm, the parameters were set as follows: initial learning rate = 10^{-4}, $\beta1 = 0.9$, $\beta2 = 0.999$, $\varepsilon = 10^{-5}$ without applying dropout, and number of epochs = 150. After training, $CBCT_{25\%}$ was used as the input for U-net, and the corresponding $CBCT_{25\%+DCNN}$ was generated for each patient. In this study, the $CBCT_{100\%}$ was treated as the ground truth. In addition, the impact of sample size on the training was

investigated. Five, ten, and fourteen patients were randomly selected and training was performed with the same network parameters. All calculations were performed using a single GeForce RTX 2080 GPU with 8 GB memory, and the training was conducted with a mini-batch size of 8.

2.4. Voxel value deviations and image quality evaluation

As the XVI 4.2.2 cannot be calibrated in Hounsfield Unit (HU), we did not evaluate the accuracy of the HU itself. We used mean absolute error (MAE) to evaluate the difference in voxel values between the input images and the images generated by the DCNN. Planning CT and CBCT were registered with bony structures or the prostate itself. The regions of interest (ROIs) were set to the prostates and femoral heads to evaluate local voxel value deviations as shown in Figure 3. The MAE of voxel values in each ROI was calculated as

$$\mathrm{MAE} = \frac{1}{N}\sum_{i=1}^{N}\left|Y_{eval}(v_i) - Y_{ref}(v_i)\right|, \quad (1)$$

where v_i is the i-th voxel, and N is the total number of voxels within the ROI. Y_{evel} is the evaluation value (voxel values in $\mathrm{CBCT}_{25\%}$, $\mathrm{CBCT}_{50\%}$, and $\mathrm{CBCT}_{25\%+\mathrm{DCNN}}$), and Y_{ref} is the reference value (voxel values in $\mathrm{CBCT}_{100\%}$).

The obtained $\mathrm{CBCT}_{25\%}$, $\mathrm{CBCT}_{50\%}$, and $\mathrm{CBCT}_{25\%+\mathrm{DCNN}}$ were also evaluated by the peak signal-to-noise ratio (PSNR) and structural similarity (SSIM) [24]. PSNR is derived from the mean square error and indicates the ratio of the maximum pixel intensity to the power of the distortion. The SSIM is a human visual system-based metric that evaluates different attributes such as luminance, contrast, and structure comprehensively. The PSNR and SSIM of CBCTs were measured based on $\mathrm{CBCT}_{100\%}$, and their average values over 120 slices were evaluated for each patient. The workflow used to evaluate the voxel value deviations and image quality for the $\mathrm{CBCT}_{25\%+\mathrm{DCNN}}$ is shown in Figure 4.

3. Results

Figure 5 shows the voxel value histogram of the original CBCT and $\mathrm{CBCT}_{100\%}$ in the body region. The mean error between these images was 5.65 ± 18.5. The model was trained for 15.3 h per subject. Thus, the training required approximately 91.7 h to perform the sixfold cross-validation for 36 patients. Figure 6 shows one case of the training and test loss (mean

absolute error) over each epoch. The model converged and both training and test data performance were equivalent. After the model was trained, approximately 6.4 s (0.05 s per slice) was required to convert a new patient $CBCT_{25\%}$ dataset to the $CBCT_{25\%+DCNN}$ images. Figure 7 shows two different slices of $CBCT_{25\%}$, $CBCT_{50\%}$, and $CBCT_{25\%+DCNN}$ images for patient number 16. Improvement can be seen in terms of noise and artifacts.

Table 2 lists the MAE, SSIM, and PSNR in the prostate and femoral head regions of each patient. Figure 8 shows a histogram of the absolute error between each CBCT image and $CBCT_{100\%}$ in the prostate and femoral head regions for a patient. The average MAE over all patients in the femoral head region for $CBCT_{25\%}$, $CBCT_{50\%}$, and $CBCT_{25\%+DCNN}$ were 26.7±4.73, 15.2±3.31, and 13.9±2.46, respectively. The corresponding values in the prostate region for $CBCT_{25\%}$, $CBCT_{50\%}$, and $CBCT_{25\%+DCNN}$ were 22.6±3.56, 12.6±2.78, and 12.0±2.85, respectively. The MAE of $CBCT_{25\%+DCNN}$ was small in both the prostate and bone regions in comparison with that of $CBCT_{25\%}$ (p-value < 0.01; Wilcoxon rank sum test). In contrast, there was no significant difference between the MAE of $CBCT_{50\%}$ and that of $CBCT_{25\% + DCNN}$ in both regions (p-value = 0.01 and 0.04; Wilcoxon rank sum test). On average, the SSIMs of $CBCT_{25\%}$, $CBCT_{50\%}$, and $CBCT_{25\%+DCNN}$ were 0.94±0.02, 0.98±0.01, and 0.98±0.01, respectively. In terms of PSNR, $CBCT_{25\%}$, $CBCT_{50\%}$, and $CBCT_{25\%+DCNN}$ were 45.3±1.13 dB, 51.6±2.03 dB, and 52.8±1.68 dB, respectively. SSIM and PSNR for the $CBCT_{50\%}$ were larger than those for the $CBCT_{25\%+DCNN}$ (p-value < 0.01; Wilcoxon rank sum test). This shows that the image quality of $CBCT_{25\%+DCNN}$ is comparable to that of $CBCT_{50\%}$. Figure 9 shows the SSIM and PSNR of $CBCT_{25\% + DCNN}$ for patient number 7 using the model trained by 5, 10, 14, and 30 patients. The SSIM and PSNR increased depending on the number of training data.

4. Discussion

We applied a DCNN to generate high-quality and high-speed CBCT images to learn direct mappings from $CBCT_{25\%}$ to their corresponding $CBCT_{100\%}$. $CBCT_{25\%+DCNN}$ was comparable to $CBCT_{50\%}$. Westberg et al. [11] reported that the accuracy of $CBCT_{50\%}$ is sufficient with respect to IGRT. Thus, we concluded that $CBCT_{25\%+DCNN}$ can be used for IGRT for prostate cancer. In fact, Kida et al. [21] reported an improvement in the image quality of CBCT images following application of U-net to learn mappings from CBCT images to their corresponding planning CT images for prostate cancer. The PSNR and SSIM

of those images generated by U-net were 53.0 dB and 0.98 at maximum, respectively. Although not directly comparable with the results of this method in modalities, our results meet the criteria of related studies. In terms of MAE, SSIM, and PSNR, there were no significant differences between $CBCT_{50\%}$ and $CBCT_{25\% + DCNN}$.

A Phase III trial comparing the effectiveness of daily and weekly IGRT for prostate cancer shows that daily IGRT reduces the risk of biochemical recurrences, clinical recurrences, and rectal toxicity compared with weekly IGRT [4]. However, daily IGRT causes higher exposure dose to normal organs [8], and currently, it is not commonly used in clinical routine. Our method would be helpful in changing this situation. Reducing the number of projections used for reconstruction to 25% is equivalent to reducing the dose to 25% because the frequency of the projection data acquisition is constant. In other words, this study indicates that noise and artifacts reduction using DCNN can reduce exposure to almost one quarter of conventional exposure without sacrificing the image quality required for IGRT. In addition, it is possible that the CBCT scan speed can be increased by a factor of four without sacrificing the image quality required for IGRT. Speeding up the CBCT scanning can improve the treatment quality for individual patients and total patient throughput. It may also enable single breath-hold CBCT scans [12-14]. Whereas the fast gantry rotation of conventional linac could pose a collision hazard to patients, the ring gantry type linac should not be a problem in this regard.

One of the limitations of this study is the small sample size used; therefore, the DCNN model was evaluated using the sixfold cross-validation method. In addition, the SSIM and PSNR increased with the number of samples used for training (i.e., 5, 10, 14, and 30 patients). This means that the image quality of $CBCT_{25\% + DCNN}$ would further improve if the number of samples used for training was larger than that used in this study. However, it should be noted that overfitting of the training data did not occur in this study, although the number was relatively small. We constructed a 2D DCNN model because of the limitations of GPU memory and number of training data. The accuracy would be further improved by using more advanced network architectures such as 3D DCNN and generative adversarial network. By increasing the training data, it may be possible to improve the image quality of the reconstructed images with a smaller amount of projection data. Furthermore, adding additional anatomical information in the training data such as the manually delineated contour of bony structures or prostate for the U-net can further improve the estimation accuracy. Further research is required for the proposed method to be applied to other organs

such as the chest, head, and neck [20]. This study only used pelvic images for improving IGRT in the treatment of prostate cancer.

The DCNN cannot remove an artifact included in both $CBCT_{25\%}$ and $CBCT_{100\%}$. In fact, there is an artifact close to the couch in proximity to a patient's skin with $CBCT_{25\%+DCNN}$ because couch correction was not applied in the reconstruction process (see Figure 7 for $CBCT_{25\%}$ and $CBCT_{100\%}$. However, this artifact would not affect IGRT accuracy because planning CT and CBCT are generally registered with the bony structure or prostate itself. Another limitation is the reconstruction process of the evaluated CBCT images, which does not incorporate the inherent weaknesses of CBCT. For example, CBCT has greater inter-slices correlation and artifacts with reference to multislice CT. Westberg et al. [11] "deactivated" projections from the original CBCT raw data prior to reconstruction to simulate high-speed CBCT, and the reconstruction was made using an Elekta CBCT projector. In contrast, we first projected the original CBCT images from the XVI system and then reconstructed CBCT images using different numbers of projection data with the scikit-image image processing library. As the reconstruction algorithm used in this procedure is different from the original Elekta's reconstruction algorithm, the obtained CBCT images were not perfectly identical to the real CBCT images. As shown in Figure 5, there is no significant difference between these images. On the other hand, there is no guarantee that $CBCT_{25\%}$ and $CBCT_{50\%}$ will match the CBCT images made via "deactivated" projections from original CBCT images. Further, the results of our study cannot be generalized because it depends on the number of projections used for the reconstruction of $CBCT_{100\%}$. Currently, commonly used CBCT systems have >300 projections, whereas 480 projections were used in this study. As the number of projections decreases, so does the image quality of $CBCT_{100\%}$, $CBCT_{50\%}$, and $CBCT_{25\%}$. In such a case, it is unclear how much the image quality could be improved by using a DCNN.

Reducing the imaging dose of CBCT is not a major advantage in stereotactic irradiation with a small number of fractions. 4D-CBCT is often used to assess the movement of liver and lung tumors during stereotactic body radiation therapy [25, 26], with 4D-CBCT consisting of ten phase images being reconstructed from the projection data of each phase. Smaller amounts of projection data, therefore, are used for reconstruction than for normal CBCT, leading to image quality degradation [25]. As shown by the results of the present study, we can expect to reduce noise and artifacts in 4D-CBCT using a DCNN.

5. Conclusion

We developed a DCNN model for removing noise and artifacts from high-speed CBCT. An evaluation of the image quality and HU deviations demonstrated that $CBCT_{25\%+DCNN}$ is sufficient for the required IGRT accuracy. We established that it is possible to reduce exposure to one quarter without sacrificing the quality required for IGRT and to increase the CBCT scan speed to a factor of four. Future work will include improvement of the process for simulating high-speed CBCT and further evaluation of the proposed method on larger datasets incorporating other anatomical regions.

Conflict of interest disclosure

The authors have no conflict of interest to disclose.

Funding

This work was supported by a Grant-in-Aid for JSPS Research Fellow [grant number JP18J22705].

References

[1] Wortel RC, Incrocci L, Pos FJ, Lebesque JV, Witte MG, van der Heide UA, et al. Acute toxicity after image-guided intensity modulated radiation therapy compared to 3D conformal radiation therapy in prostate cancer patients. Int J Radiat Oncol Biol Phys. 2015;91:737-44.

[2] Sveistrup J, af Rosenschold PM, Deasy JO, Oh JH, Pommer T, Petersen PM, et al. Improvement in toxicity in high risk prostate cancer patients treated with image-guided intensity-modulated radiotherapy compared to 3D conformal radiotherapy without daily image guidance. Radiat Oncol. 2014;9:44.

[3] Singh J, Greer PB, White MA, Parker J, Patterson J, Tang CI, et al. Treatment-related morbidity in prostate cancer: a comparison of 3-dimensional conformal radiation therapy with and without image guidance using implanted fiducial markers. Int J Radiat Oncol Biol Phys. 2013;85:1018-23.

[4] de Crevoisier R, Bayar MA, Pommier P, Muracciole X, Pene F, Dudouet P, et al. Daily Versus Weekly Prostate Cancer Image Guided Radiation Therapy: Phase 3 Multicenter Randomized Trial. Int J Radiat Oncol Biol Phys. 2018;102:1420-9.

[5] Ariyaratne H, Chesham H, Pettingell J, Alonzi R. Image-guided radiotherapy for prostate cancer with cone beam CT: dosimetric effects of imaging frequency and PTV margin. Radiother Oncol. 2016;121:103-8.

[6] Tondel H, Lund JA, Lydersen S, Wanderas AD, Aksnessaether B, Jensen CA, et al. Radiotherapy for prostate cancer - Does daily image guidance with tighter margins improve patient reported outcomes compared to weekly orthogonal verified irradiation? Results from a randomized controlled trial. Radiother Oncol. 2018;126:229-35.

[7] Kim DW, Chung WK, Yoon M. Imaging doses and secondary cancer risk from kilovoltage cone-beam CT in radiation therapy. Health Phys. 2013;104:499-503.

[8] Kamath S, Song W, Chvetsov A, Ozawa S, Lu H, Samant S, et al. An image quality comparison study between XVI and OBI CBCT systems. J Appl Clin Med Phys. 2011;12:3435.

[9] Thomas SJ. Capacity and demand models for radiotherapy treatment machines. Clin Oncol (R Coll Radiol). 2003;15:353-8.

[10] Hoogeman MS, Nuyttens JJ, Levendag PC, Heijmen BJ. Time dependence of intrafraction patient motion assessed by repeat stereoscopic imaging. Int J Radiat Oncol Biol Phys. 2008;70:609-18.

[11] Westberg J, Jensen HR, Bertelsen A, Brink C. Reduction of Cone-Beam CT scan time without compromising the accuracy of the image registration in IGRT. Acta Oncologica. 2010;49:225-9.

[12] Arns A, Wertz H, Boda-Heggemann J, Schneider F, Blessing M, Abo-Madyan Y, et al. Ultrafast single breath-hold cone-beam CT lung cancer imaging with faster linac gantry rotation. Radiother Oncol. 2019;135:78-85.

[13] Arns A, Fleckenstein J, Schneider F, Steil V, Wenz F, Wertz H. SU-K-FS4-11: High-Speed KV-CBCT-Imaging with a Faster Linac Gantry Rotation: 3D Imaging Within One Breath-Hold. The American Association of Physicists in Medicine 59th Annual Meeting & Exhibition. 2017:2017/7/30.

[14] Arns A, Fleckenstein J, Schneider F, Boda-Heggemann J, Abo-Madyan Y, Steil V, et al. EP-2041: Registration accuracy of high-speed single breath-hold kV-CBCT lung cancer imaging. ESTRO 39, Electronic Poster: Physics track: Inter-fraction motion management. 2019;127:S1116.

[15] Chen H, Zhang Y, Kalra MK, Lin F, Chen Y, Liao P, et al. Low-Dose CT With a Residual Encoder-Decoder Convolutional Neural Network. IEEE Trans Med Imaging. 2017;36:2524-35.

[16] Mori S. Deep architecture neural network-based real-time image processing for image-guided radiotherapy. Phys Med. 2017;40:79-87.

[17] Zhang Y, Chu Y, Yu H. Reduction of metal artifacts in x-ray CT images using a convolutional neural network. In: Muller B, Wang G, eds. . Proc SPIE Developments in X-Ray Tomography XI. 2017;10391:103910V.

[18] Han Y, Yoo J, Kim HH, Shin HJ, Sung K, Ye JC. Deep learning with domain adaptation for accelerated projection-reconstruction MR. Magn Reson Med. 2018;80:1189-205.

[19] Lv J, Yang M, Zhang J, Wang X. Respiratory motion correction for free-breathing 3D abdominal MRI using CNN-based image registration: a feasibility study. Br J Radiol. 2018;91:20170788.

[20] Chen S, Qin A, Zhou D, Yan D. Technical Note: U-net-generated synthetic CT images for magnetic resonance imaging-only prostate intensity-modulated radiation therapy treatment planning. Med Phys. 2018;45:5659-65.

[21] Kida S, Nakamoto T, Nakano M, Nawa K, Haga A, Kotoku J, et al. Cone Beam Computed Tomography Image Quality Improvement Using a Deep Convolutional Neural Network. Cureus. 2018;10:e2548.

[22] Sahiner B, Pezeshk A, Hadjiiski LM, Wang X, Drukker K, Cha KH, et al. Deep learning in medical imaging and radiation therapy. Med Phys. 2019;46:e1-e36.

[23] van der Walt S, Schonberger JL, Nunez-Iglesias J, Boulogne F, Warner JD, Yager N, et al. scikit-image: image processing in Python. PeerJ. 2014;2:e453.

[24] Wang Z, Bovik AC, Sheikh HR, Simoncelli EP. Image quality assessment: from error visibility to structural similarity. IEEE Trans Image Process. 2004;13:600-12.

[25] Sonke JJ, Zijp L, Remeijer P, van Herk M. Respiratory correlated cone beam CT. Med Phys. 2005;32:1176-86.

[26] Shimohigashi Y, Araki F, Maruyama M, Yonemura K, Nakaguchi Y, Kai Y, et al. Image quality of four-dimensional cone-beam computed tomography obtained at various gantry rotation speeds for liver stereotactic body radiation therapy with fiducial markers. Phys Med. 2018;45:19-24.

Figure legends

Figure 1 Procedure for reconstructing each CBCT. The original CBCT images were projected by the Radon transform, and 480 imaginary projection data were created. Three types of CBCT images were reconstructed from the projection data. The CBCT images reconstructed from 480, 240, and 120 projection data were defined as $CBCT_{100\%}$, $CBCT_{50\%}$, and $CBCT_{25\%}$, respectively.

Figure 2 U-net convolutional neural network architecture.

Figure 3 Setting of ROIs for prostate and bone. The yellow circles placed on the axial view were selected as $ROI_{Prostate}$ and ROI_{Bone} for the MAE calculation.

Figure 4 Workflow to evaluate the HU deviations and image quality for each CBCT image. PSNR, SSIM, and MAE of CBCTs were calculated in comparison with the values of $CBCT_{100\%}$. Average values of PSNR and SSIM over 120 slices were evaluated for each patient.

Figure 5 Comparison of $CBCT_{100\%}$ and original CBCT for one case. (a) $CBCT_{100\%}$, (b) original CBCT, and (c) voxel value histogram of $CBCT_{100\%}$ and original CBCT for all slices (120 slices) in body region.

Figure 6 One case of learning curves on the training data (30 patients) and test data (1 patient).

Figure 7 Subtraction images between each CBCT image and reference image at two different slice positions (patient number 16).

Figure 8 Histogram of absolute error between each CBCT image and $CBCT_{100\%}$ in the (a) prostate and (b) femoral head regions (patient number 8).

Figure 9 SSIM and PSNR of $CBCT_{25\%+DCNN}$ of patient number 27 using the model trained by 5, 10, 14, and 30 patients.

Table 1 List of the relevant parameters used during scanning with the XVI

Protocol	Pelvis
kV collimator	M20
kVp	120
(mA, ms/frame)	(40, 40)
Acquisition gantry angle	183 deg. to 179 deg.
Acquisition time	~120 s

Table 2 Quantitative analysis of the image qualities for the 36 cases.

Mean ± SD	MAE		SSIM	PSNR
	ROI_{Bone}	$ROI_{Prostate}$		
$CBCT_{25\%}$	26.7±4.73	22.6±3.56	0.94±0.02	45.3±1.13
$CBCT_{50\%}$	15.2±3.31	12.6±2.78	0.98±0.01	51.6±2.03
$CBCT_{25\%+DCNN}$	13.9±2.46	12.0±2.85	0.98±0.01	52.8±1.68

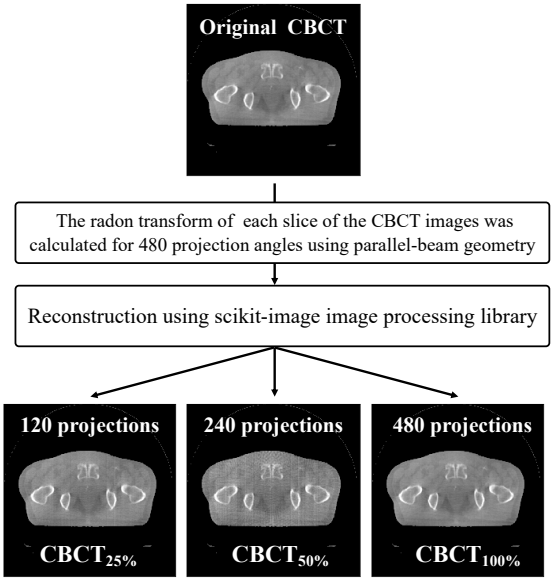

Figure 1 Procedure for reconstructing each CBCT. The original CBCT images were projected by the Radon transform, and 480 imaginary projection data were created. Three types of CBCT images were reconstructed from the projection data. The CBCT images reconstructed from 480, 240, and 120 projection data were defined as $CBCT_{100\%}$, $CBCT_{50\%}$, and $CBCT_{25\%}$, respectively.

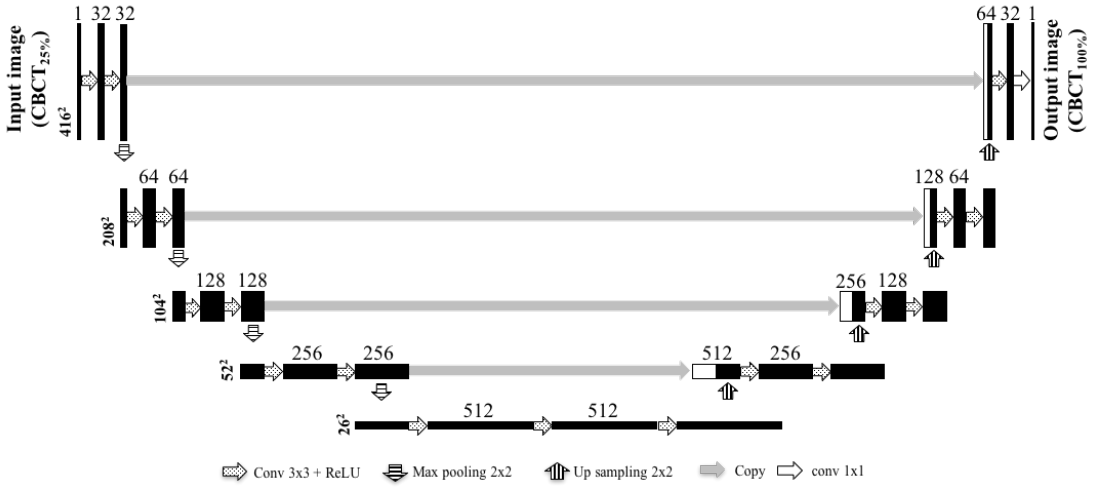

Figure 2 U-net convolutional neural network architecture.

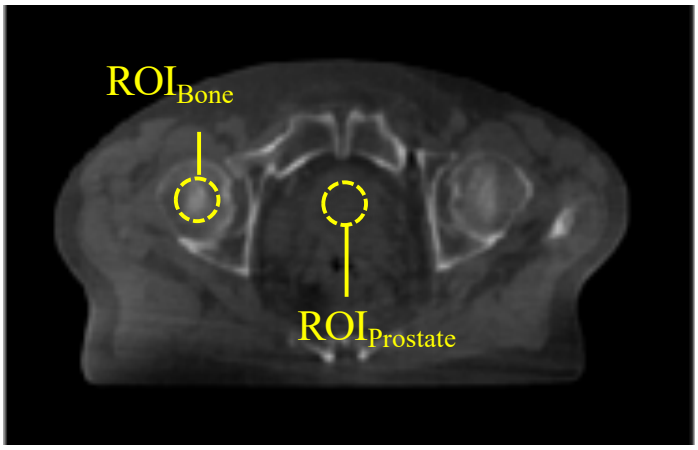

Figure 3 Setting of ROIs for prostate and bone. The yellow circles placed on the axial view were selected as $ROI_{Prostate}$ and ROI_{Bone} for the MAE calculation.

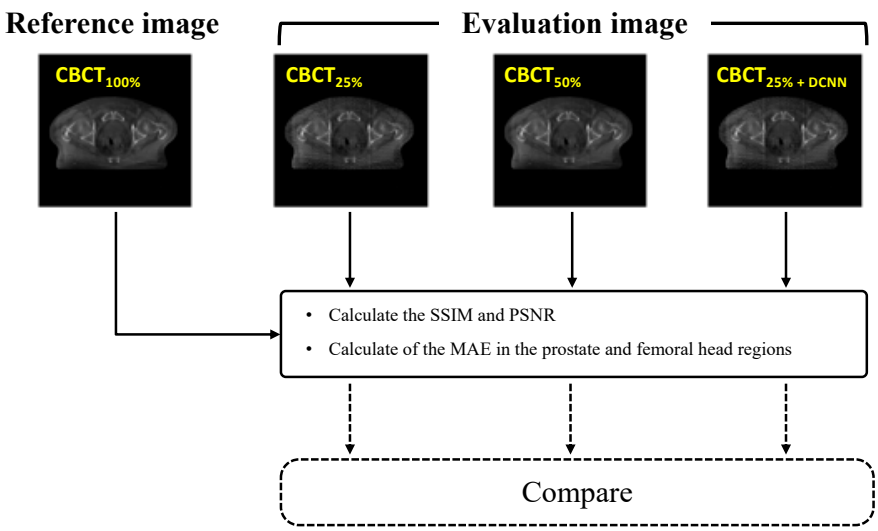

Figure 4 Workflow to evaluate the HU deviations and image quality for each CBCT image. PSNR, SSIM, and MAE of CBCTs were calculated in comparison with the values of $CBCT_{100\%}$. Average values of PSNR and SSIM over 120 slices were evaluated for each patient.

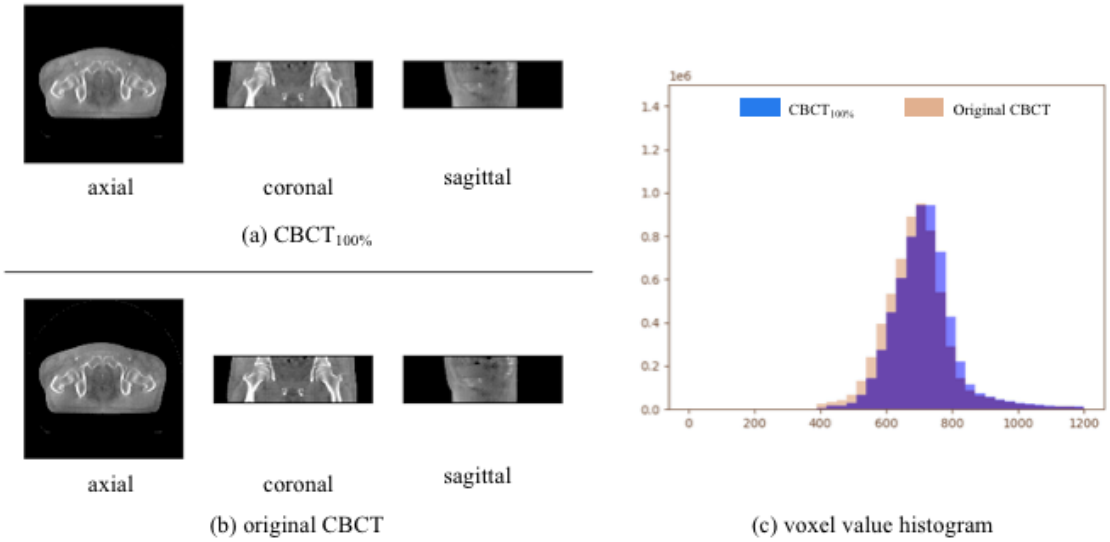

Figure 5 Comparison of $CBCT_{100\%}$ and original CBCT for one case. (a) $CBCT_{100\%}$, (b)original CBCT, and (c) voxel value histogram of $CBCT_{100\%}$ and original CBCT for all slices (120 slices) in body region.

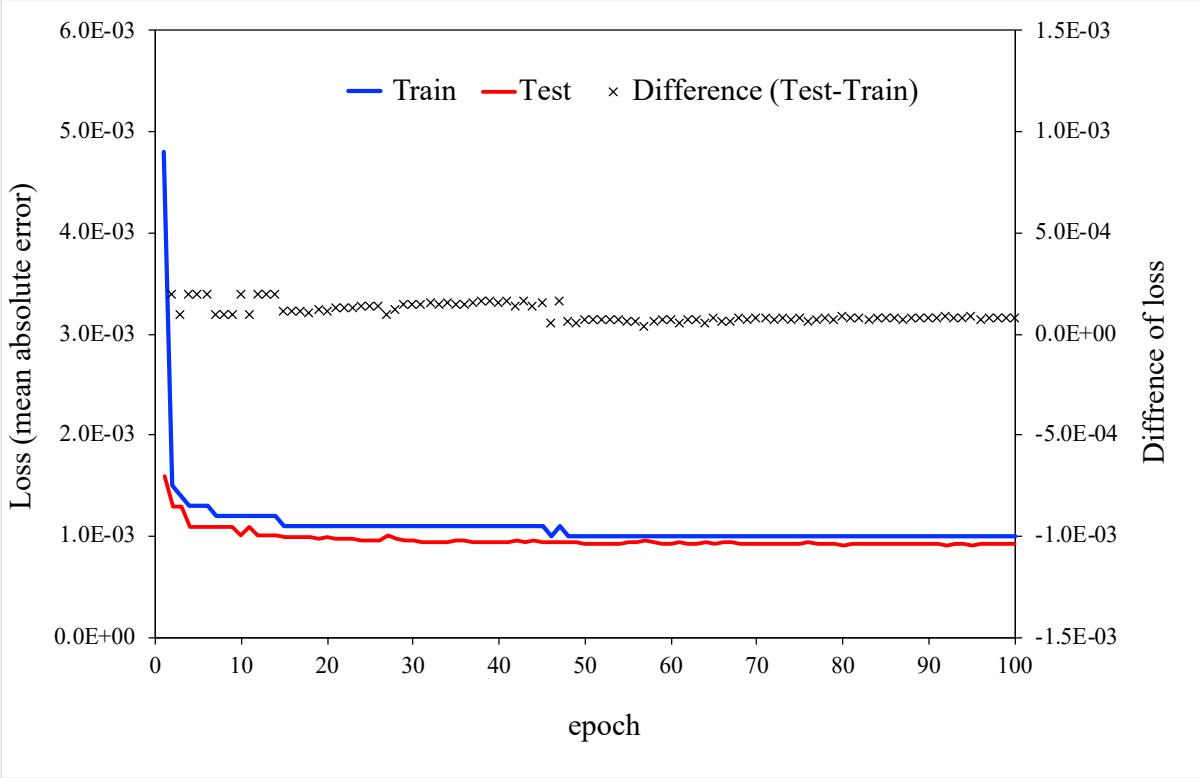

Figure 6 One case of learning curves on the training data (30 patients) and test (1 patient).

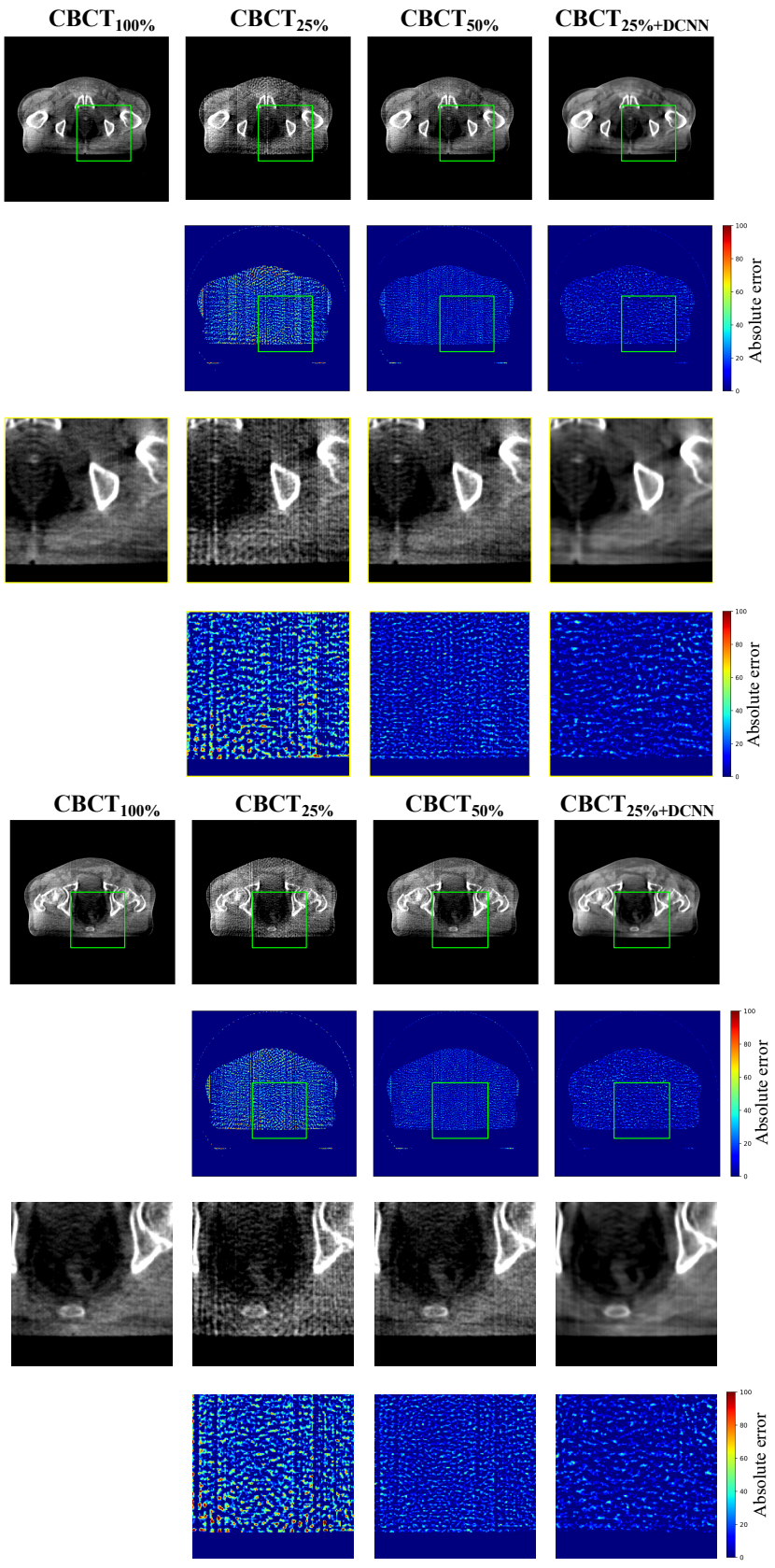

Figure 7 Subtraction images between each CBCT image and reference image at two different slice positions (patient number 16).

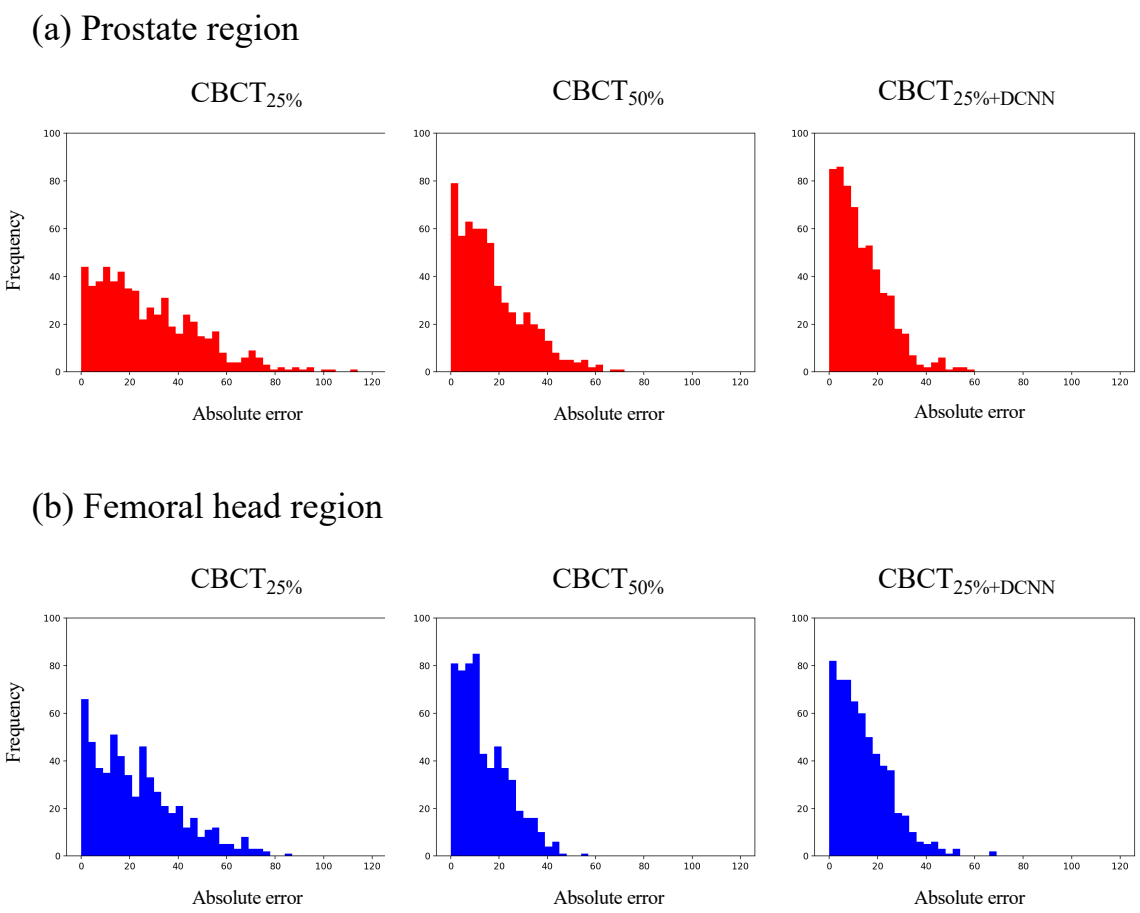

Figure 8 Histogram of absolute error between each CBCT image and $CBCT_{100\%}$ in the (a) prostate and (b) femoral head regions (patient number 8).

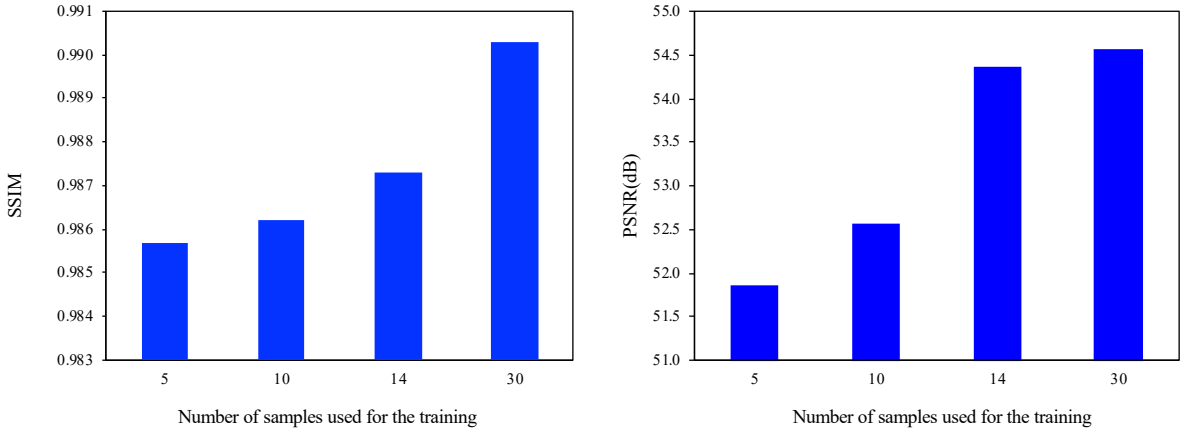

Figure 9 SSIM and PSNR of $CBCT_{25\% + DCNN}$ of patient number 27 using the model trained by 5, 10, 14, and 30 patients.